**RAA 2019** Vol. **19** No. **3**, 47(10pp) doi: 10.1088/1674–4527/19/3/47

*http://www.raa-journal.org* *http://iopscience.iop.org/raa*

***R**esearch in*
***A**stronomy and*
***A**strophysics*

# Calibration of the *DAMPE* Plastic Scintillator Detector and its on-orbit performance

Meng Ding[1,2], Ya-Peng Zhang[1⋆], Yong-Jie Zhang[1], Yuan-Peng Wang[3,4], Tie-Kuang Dong[3], Antonio De Benedittis[5,6], Paolo Bernardini[5,6], Fang Fang[1], Yao Li[1,2], Jie Liu[1], Peng-Xiong Ma[3,4], Zhi-Yu Sun[1], Valentina Gallo[7], Stefania Vitillo[7], Zhao-Min Wang[8,9], Yu-Hong Yu[1], Chuan Yue[3,4], Qiang Yuan[3], Yong Zhou[1,2] and Yun-Long Zhang[10]

[1] Institute of Modern Physics, Chinese Academy of Sciences, Lanzhou 730000, China; *y.p.zhang@impcas.ac.cn*
[2] University of Chinese Academy of Sciences, Beijing 100049, China
[3] Key Laboratory of Dark Matter and Space Astronomy, Purple Mountain Observatory, Chinese Academy of Sciences, Nanjing 210008, China
[4] School of Astronomy and Space Science, University of Science and Technology of China, Hefei 230026, China
[5] Istituto Nazionale di Fisica Nucleare (INFN) - Sezione di Lecce, I-73100 Lecce, Italy
[6] Dipartimento di Matematica e Fisica E. De Giorgi, Università del Salento, I-73100 Lecce, Italy
[7] Department of Nuclear and Particle Physics, University of Geneva, CH-1211 Geneva, Switzerland
[8] Gran Sasso Science Institute, Via M. lacobucci 2, 67100 L'Aquila, Italy
[9] INFN Laboratori Nazionali del Gran Sasso, 67100 L'Aquila, Italy
[10] Department of Modern Physics, University of Science and Technology of China, Hefei 230026, China

Received 2018 July 9; accepted 2018 October 16

**Abstract** The *DArk Matter Particle Explorer* (*DAMPE*) is a space-borne apparatus for detecting the high-energy cosmic-ray-like electrons, $\gamma$-rays, protons and heavy ions. The Plastic Scintillator Detector (PSD) is the top-most sub-detector of the *DAMPE*. The PSD is designed to measure the charge of incident high-energy particles and it also serves as a veto detector for discriminating $\gamma$-rays from charged particles. In this paper, a PSD on-orbit calibration procedure is described, which includes the five steps of pedestal, dynode correlation, response to minimum-ionizing particles, light attenuation function and energy reconstruction. A method for reconstructing the charge of incident high energy cosmic-ray particles is introduced. The detection efficiency of each PSD strip is verified to be above 99.5%; the total efficiency of the PSD for charged particles is above 99.99%.

**Key words:** cosmic ray — instrumentation: *DAMPE* — charge measurement — plastic scintillator detector calibration

## 1 INTRODUCTION

Exploring the nature of dark matter has been one of the most important topics in fields including cosmology, astrophysics and particle physics. Precisely measuring the energy spectra of cosmic-rays is vital for constraining the cosmic-ray production mechanism (Drury 2012) and their propagation in the stellar medium (Grenier et al. 2015). Measuring the energy spectrum of cosmic particles like $e^{\pm}$, $\gamma$-rays and anti-particles in space is one of the experimental methods used to constrain the properties of dark matter (Chang et al. 2008). Space-borne experiments have been pioneered by PAMELA (Picozza et al. 2010), *Fermi*-LAT (Atwood et al. 2009) and AMS-02 (Alpat et al. 2005). The *DArk Matter Particle Explorer* (*DAMPE*) (Chang et al. 2017) is a high-resolution multi-purpose device for detecting cosmic-rays including electrons, $\gamma$-rays, protons and heavy ions in an energy range of a few GeV to 100 TeV.

⋆ Corresponding Author.

*DAMPE* was launched on 2015 December 17 and operates on a sun-synchronous orbit at an altitude of 500 km.

*DAMPE* consists of four sub-detectors: a Plastic Scintillator Detector (PSD) (Yu et al. 2017), a Silicon-Tungsten Tracker (STK) (Azzarello et al. 2016), a Bismuth Germanate Oxide Calorimeter (BGO) (Zhang et al. 2015, 2016; Feng et al. 2015) and a NeUtron Detector (NUD) (He et al. 2016). The structure of *DAMPE* is shown in Figure 1.

The on-orbit calibration of the PSD is an important step in obtaining the charge information of incident particles. In this paper, after a brief introduction (Section 2) to the PSD, the PSD on-orbit calibration procedure is described in Section 3 including pedestal, dynode, minimum-ionizing particle (MIP) response, light attenuation and energy reconstruction. A charge reconstruction method and the PSD detection efficiency are presented in Section 4 and Section 5, respectively.

## 2 DESIGN OF THE PSD

The PSD is designed to fulfill two major tasks: (a) to measure the charge of incident high-energy particles with charge number $Z$ from 1 to 26; (b) to serve as a veto detector for discriminating $\gamma$-rays from charged particles. All these require the PSD to have a large dynamic range, good energy resolution and high detection efficiency.

The PSD has two layers of plastic scintillator arrays, as shown in Figure 2. Each layer is composed of 41 plastic scintillator bars and the dimensions of the bars are 884 mm $\times$28 mm (25 mm for bars on edges) $\times$10 mm. The bars in the top and bottom layers are parallel to the $X$-axis and the $Y$-axis of the *DAMPE* coordinate system, respectively. In order to avoid the ineffective detection area, neighboring bars in each layer are staggered by 8 mm, as shown in Figure 3. The active area of the PSD is 825 mm$\times$825 mm. Scintillation light of each PSD bar is collected by two Photo Multiplier-Tubes (PMTs) at two ends. Each PMT (Hamamatsu R334) has 10 dynodes.

In order to cover an energy measurement from 0.1 to 1600 energy deposition of minimum-ionizing protons (EMIPs), signals from dynode 5 and dynode 8 of each PMT are extracted. The signal of dynode 5 with smaller gain covers from four EMIPs to 1600 EMIPs and the signal of dynode 8 with bigger gain covers from 0.1 EMIPs to 40 EMIPs (Zhou et al. 2016). Overlapping measurements by two dynodes are designed to calibrate the response of a PMT. More detailed information about the design, assembly and laboratory tests has been given in Yu et al. (2017). In order to obtain stable on-orbit performance of the PSD,

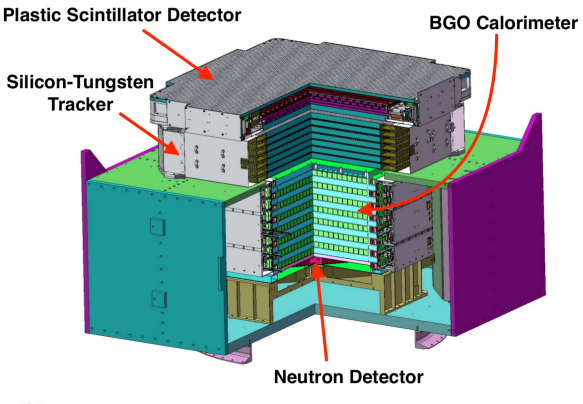


**Fig. 1** Layout of the *DAMPE* detector.

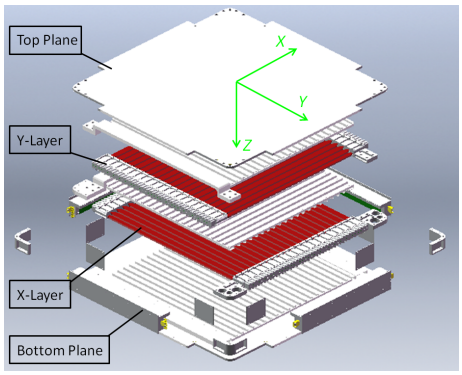


**Fig. 2** The structure of the PSD.

**Fig. 3** Side view of the PSD bars.

an active temperature control strategy was implemented by using front-end electronic boards and additional heat coils as thermal sources (Yu et al. 2017). The on-orbit temperature variation of the PSD is verified to be less than 1°C (Li et al. 2017), which is a crucial factor for maintaining stable performance of the PSD.

## 3 PSD ON-ORBIT CALIBRATION

PSD on-orbit calibration is the procedure to process PSD-associated ADCs to deposited energies, taking noise and non-linearities in actual detection processes into account. When a charged particle passes through a plastic scintillator bar, the deposited energy would be transformed into scintillation lights. The lights are collected by PMTs attached at both ends, and then the lights are converted into electronic signals. After amplification, shaping and holding etc., the amplitudes of electronic signals are recorded by ADC units. The PSD calibration procedure is quite sim-

ilar to reverse these processes, including calibration of the pedestal, dynode correlation, response to MIPs, light attenuation function and energy reconstruction. In PSD on-orbit calibration, the data collected in the South Atlantic Anomaly (SAA) region are excluded. The calibration steps mentioned above will be presented in the following subsections.

### 3.1 Pedestal Calibration

The pedestal of each readout channel is sampled twice per orbit under random triggers. The pedestal distribution of each channel is a Gaussian-like distribution. Figure 4 shows a typical pedestal distribution of a readout channel; the Gaussian fit-function is depicted by the red solid curve. The obtained pedestals (mean value of the fitted Gaussian function) and standard deviation (Gaussian $\sigma$) of each readout channel of the PSD are written into a pedestal calibration file with a time tag associated to the input data.

PSD on-orbit pedestals are almost the same as those measured before the launch of *DAMPE*. As an example, Figure 5 shows pedestals of all readout channels of the positive side of X-layer (including four spare channels) before (circles) and after (triangles) the launch of the *DAMPE*. In order to characterize the on-orbit pedestal stability of the PSD, a percentage variation of a pedestal is defined as (PED-Mean)/Mean, where PED is the pedestal of a readout channel on a different date and Mean is the average pedestal of the same channel.

Figure 6 shows the percentage variation of pedestals versus date, and each horizontal line represents a readout channel. The corresponding information for the channel, i.e. layer (L), bar (B), side (S), dynode number (Dy) and offset are listed at the right side of the figure. The offset is introduced for display reasons only. In general, the pedestals of all PSD readout channels are stable and the overall variation is less than 0.1% during the first 18 months of data-taking. PSD pedestals are updated daily, and they are then subtracted from the on-orbit data.

### 3.2 Dynode Calibration

As mentioned in Section 2, each PSD PMT gives two signals from its dynode 5 (Dy5) and dynode 8 (Dy8) in order to achieve a large dynamic range. Typically, ADC values of Dy5 and Dy8 of a PMT have a linear correlation before the Dy8 gets saturated. In order to obtain the correlation of Dy5 and Dy8 with less bias, the dynode calibration is made via a two-step iteration. In the first iteration, the correlation of Dy8 and Dy5 for each PMT is built, and it is then fitted with a linear function. A typical correlation of Dy8 and Dy5 of a PMT is shown in Figure 7, the linear fit-function is depicted by the red line, where $p_0$ and $p_1$ are the fitting parameters.

Then, Dy8 is expressed as a linear function of Dy5, and the slope parameter ($k_0 = 1/p_0$) and the intercept parameter ($b_0 = -p_1/p_0$) are obtained (the reason for obtaining values of the above parameters in such a way is that the fitting range for Dy8 is more straightforward than that of Dy5).

In the second iteration, the slope parameter of the dynode correlation is calculated by $k_1 = (\mathrm{Dy8} - b_0)/\mathrm{Dy5}$. Figure 8 shows the distribution of calculated slope parameters ($k_1$) of a PMT, which is fitted with a Gaussian distribution shown by the red solid curve. The mean ($k_{\mathrm{mean}}$) and the standard deviation ($\sigma_k$) of the fitted Gaussian function are extracted. In order to exclude abnormal events, the events within $|k_1 - k_{\mathrm{mean}}| < 5\sigma_k$ are selected, by using the slope parameter $k$ and intercept parameter $b$ which are obtained for each PMT just as the first iteration.

With the final obtained dynode calibration parameters, two ADC measurements of each PSD PMT are combined into a single ADC value, which is expressed as Equation (1),

$$\mathrm{ADC} = \begin{cases} \mathrm{ADC_{Dy8}} & \mathrm{ADC_{Dy8}} \leq 11000 \\ k \times \mathrm{ADC_{Dy5}} + b & \mathrm{ADC_{Dy8}} > 11000\ , \end{cases} \quad (1)$$

where $\mathrm{ADC_{Dy5}}$ and $\mathrm{ADC_{Dy8}}$ are the ADC values associated to Dy5 and Dy8 of a PMT, respectively.

The left panel of Figure 9 shows the percentage variation of the slope parameter versus time. The percentage variation of the slope parameter is defined in the same way as that of the pedestal (see Fig. 6). The slope percentage variation of all channels listed in the left panel of Figure 9 is shown in the right panel of Figure 9; the overall change of the slope parameter in this time period is about 0.42%. The dynode calibration is made on a daily base. In this step, the linearity of Dy8 can be controlled by the measurements from Dy5, while Dy5 may also become non-linear at large ADC values, when Dy8 is saturated. The influence of this effect will be further considered in Section 4.

### 3.3 Response of MIPs and Energy Reconstruction

Each PSD bar provides two ADC measurements from its left and right sides ($\mathrm{ADC^{L/R}}$) after the dynode calibration, and a combined ADC of each PSD bar is constructed via the geometrical average of $\mathrm{ADC^L}$ and $\mathrm{ADC^R}$, i.e. $\mathrm{ADC^C} = \sqrt{\mathrm{ADC^L} \times \mathrm{ADC^R}}$. Due to the light attenuation in the scintillator bar, the combined quantity $\mathrm{ADC^C}$ has

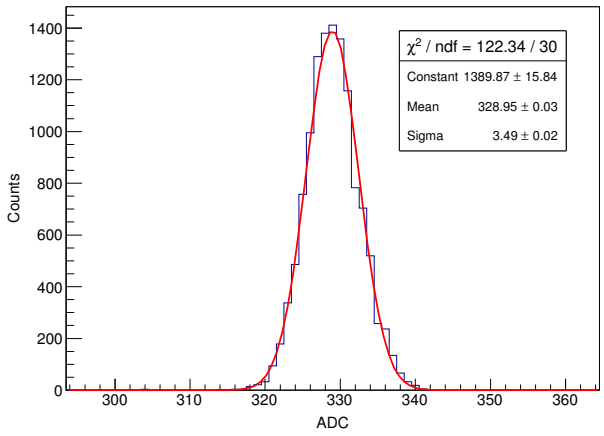


**Fig. 4** A typical pedestal distribution of a readout channel, the fitted Gaussian function is depicted by the *red solid curve*.

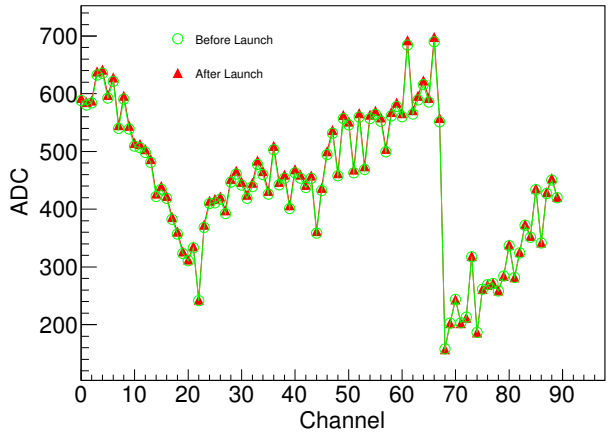


**Fig. 5** Pedestal before (*green circles*) and after (*red triangles*) the launch of *DAMPE*.

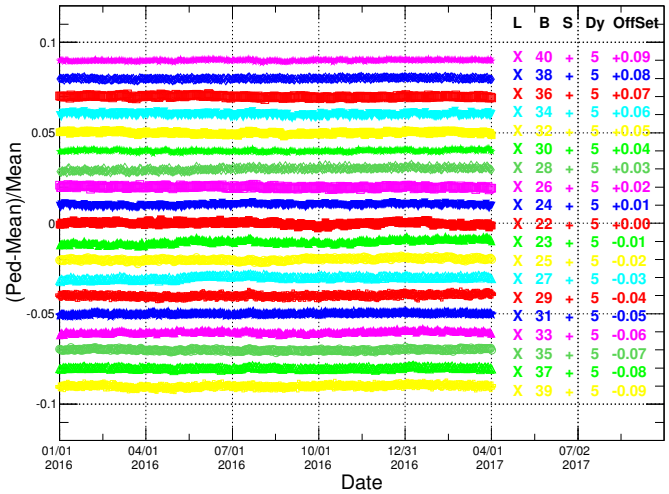


**Fig. 6** Percentage variation of pedestals versus date (an offset is introduced for display reasons).

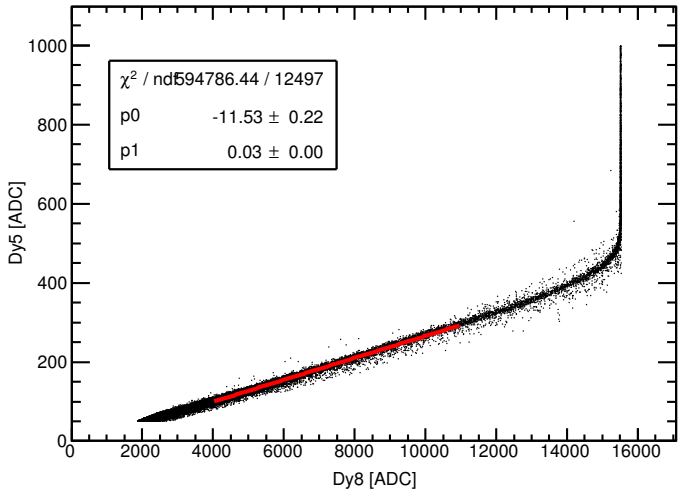


**Fig. 7** Dy5 (vertical axis) and Dy8 (horizontal axis) of a PSD PMT; the *red line* is the linear fit-function in the first iteration.

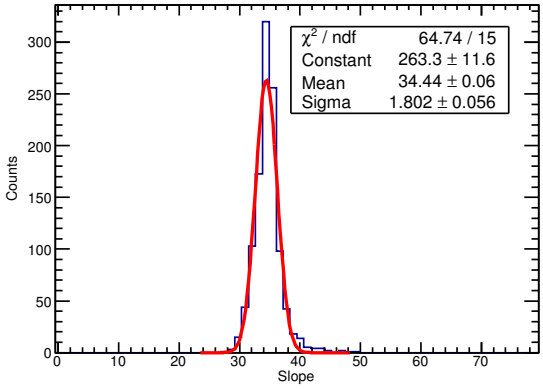


**Fig. 8** Distribution of calculated slope parameters ($k_1$) of a PMT in the second iteration.

less hit position dependence than the single-side quantities. This effect will be illustrated in subsequent sub-sections.

The events are classified as MIP events if incident particles pass through all BGO layers and their energy depositions in each BGO layer are in the range expected for MIPs (Wang et al. 2017). Figure 10 shows a typical ADC distribution of MIP events with path length correction (PSD alignment method will be published in another paper). Considering the detector resolution, the distribution is fitted by a Landau distribution convoluted with a Gaussian function (LG), shown by the red solid curve. The most probable value (MPV) of the fitted Landau distribution is obtained. For each PMT, MIP responses in each PSD bar, i.e. $\mathrm{MPV^L}$, $\mathrm{MPV^R}$ and $\mathrm{MPV^C}$, are obtained by fitting the corresponding $\mathrm{ADC^{L/R/C}}$ distribution with the LG function. The MPV values of each PSD bar are updated every five days. Thanks to the temperature control system, MPV values of PSD PMTs are very stable. Figure 11 shows the MPV of a PMT versus the time; MPV variation of this PMT is less than four ADC channels.

Considering the energy deposition of minimum-ionizing protons passing through the plastic scintillator is about 2 MeV $\mathrm{cm^{-1}}$ (the thickness of a PSD bar is 1 cm), the measured energies of left/right/combined sides of each PSD bar ($E^{\mathrm{L/R/C}}$) are derived according to

$$E_i^{\mathrm{L/R/C}} = \frac{\mathrm{ADC}_i^{\mathrm{L/R/C}}}{\mathrm{MPV_i^{L/R/C}}} \times 2\ \mathrm{MeV}\ , \qquad (2)$$

where $\mathrm{ADC}_i^{\mathrm{L/R/C}}$ are the ADC value of the left/right/combined side of $i$-th PSD bar.

### 3.4 Light Attenuation Calibration

The scintillation lights generated along the path of incident charged particle would attenuate during their propagation

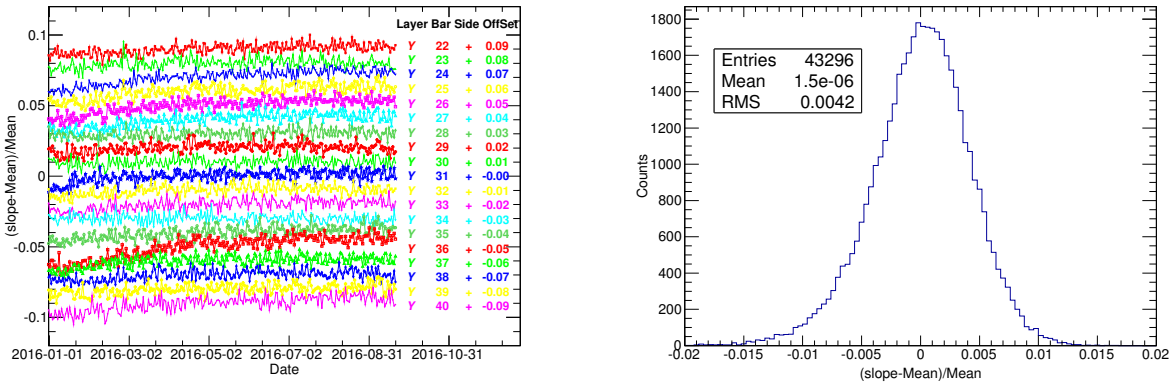


**Fig. 9** *Left panel*: Percentage variation of the slope parameter of channels versus time. *Right panel*: the overall distribution of the percentage variation of the slope parameter.

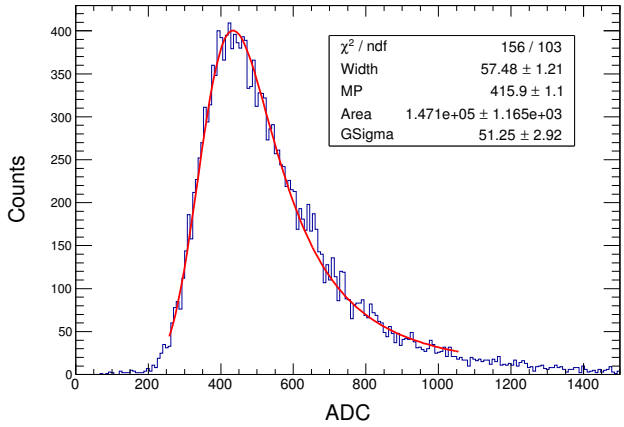


**Fig. 10** Typical ADC distribution of MIP, the *red curve* is the fitted Landau distribution convoluted with a Gaussian function.

due to light absorption and re-scattering. In general, the quantity of scintillation lights received by a PMT is inversely proportional to the distance between hit position and the PMT. Due to the light attenuation effect, the obtained energy (Eq. (2)) needs to be corrected according to the corresponding light attenuation function and the hit position.

The light attenuation behavior of each PSD bar is investigated using a sample of MIP events with an unambiguous global track (global track defined as an STK track compatible with BGO track), the hit positions are obtained by extrapolating the track to PSD sub-layers.

Figure 12 shows a typical scatter plot of the reconstructed energy of a PMT with path length correction and obtained hit position. Energy distributions of each horizontal bin of Figure 12 are obtained, and they are fitted by a Landau distribution, respectively. The obtained MPVs are shown by triangles in Figure 12. The light attenuation functions of the left/right side of the PSD strips are obtained by fitting the corresponding correlation of MPV versus hit position with a function in Equation (3), which is the linear combination of an exponential function and a 3rd-order polynomial function (EP3),

$$A(x) = C_0 e^{-x/\lambda} + C_1 + C_2 x + C_3 x^2 + C_4 x^3 \,, \quad (3)$$

where $\lambda$ and $C_0, ..., C_4$ are fitting parameters and $x$ is the hit position. The fit function is depicted by the red curve in Figure 12.

In order to take into account possible large structure(s) in the correlation of MPV versus hit position, the correlations of the left or right side of the PSD bars are smoothed by fourth-order polynomial functions in four regions (a range of neighboring regions are overlapped), respectively. The smoothed MPV at each hit position is obtained from one of the smoothing polynomial functions. Based on smoothed MPV data and hit positions, attenuation functions of each side of the PSD bars are constructed by means of the 3rd-order spline method (ROOT::TSpline). The light attenuation function for the combined energy of

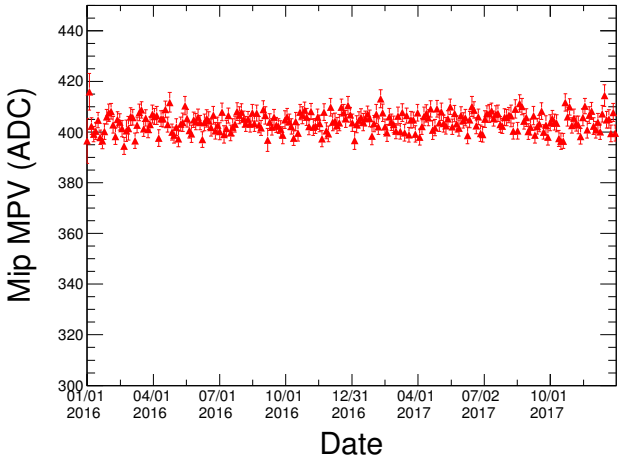


**Fig. 11** Fitted MPV value of a PMT versus the time.

a PSD bar (see Eq. (2)) is calculated from the attenuation functions of the left and right sides, i.e. $A^{\rm C}(x) = \sqrt{A^{\rm L}(x) \times A^{\rm R}(x)}$. As an example, typical light attenuation functions (MPV versus hit position) of left (triangles), right (squares) and combined (circles) sides of a PSD bar are shown in Figure 13, the fitted EP3 functions and spline functions (noted as SP3) are shown by the dashed and solid lines, respectively. Both Equation (3) and the spline function can describe well the light attenuation behaviors of PSD bars.

## 4 CHARGE RECONSTRUCTION

According to the Bethe equation (Patrignani & Particle Data Group 2016), the energy loss of charged particles in matter is proportional to the square of their electric charge, and it increases slowly with the energy when $\beta\gamma$ >4. Therefore, the charge of an incident particle can be obtained by comparing its energy deposition to that of minimum-ionizing protons.

The reconstructed charge of incident particles ($Q_{\rm rec}^{\rm L/R/C}$) could be extracted using the following expression:

$$Q_{\rm rec}^{\rm L/R/C} = \sqrt{\frac{E^{\rm L/R/C}}{A^{\rm L/R/C}(x)} \times \frac{\rm S}{l}}\,, \qquad (4)$$

where $E^{\rm L/R/C}$ is the energy of the left/right/combined sides of a PSD bar, $l$ is the path length of the particle inside the volume of the PSD bar, $S = 10$ mm is the thickness of the PSD bar, $A^{\rm L/R/C}(x)$ is the corresponding light attenuation function (see Eq. (3) and Fig. 12) and $x$ is the hit position given by the track.

Figure 14 shows the correlation between the reconstructed combined-side charge ($Q_{\rm rec}^{C}$) of the X-layer of the PSD and the hit position. The horizontal bands represent cosmic ray nuclei with different charges.

In Figure 14, reconstructed charges (different bands) at large values are not at their nominal charges. For example, the top band corresponds to Fe ($Z = 26$) while the band is located at about 20. This is mainly due to the so-called quenching effect (Winckler 1965), and partially due to the gain non-linearity of individual channels. The quenching effect represents the fact that the energy deposition of high $Z$ particles in matter is smaller than that given by the Bethe equation. Besides, signals from high $Z$ particles are measured by Dy5 of the PSD PMTs, and the gain linearities are slightly different from one readout channel to another. For these reasons, the charge spectra reconstructed by different PMTs may vary slightly.

In order to correct the above-mentioned effects, visible peaks in reconstructed charge spectra ($Q^{\rm L/R/C}$ distribution) of each PSD bar are fitted by a series of Gaussian fits, and peak positions (mean of Gaussian function) are obtained, respectively. The peaks are assigned to known cosmic-ray nuclei based on knowledge of cosmic nuclei abundance. Based on the obtained peak position and nominal charge number pairs, a third-order spline function (SP3) for each charge measurement (left/right/combined sides) of a PSD bar is constructed, respectively. For each reconstructed charge (see Eq. (4)), a quenching-effect corrected charge can be obtained from the corresponding third-order spline function. For reconstructed charge above Fe i.e. $Q_{\rm rec} > Q_{\rm rec}^{\rm Fe}$, a linear function is used to correct for the quenching effect, which is fitted from the pairs of peak position and nominal charge number with $Q_{\rm rec} > 10$. After applying this correction, the charge spectra reconstructed from different PSD bars are aligned on a bisector

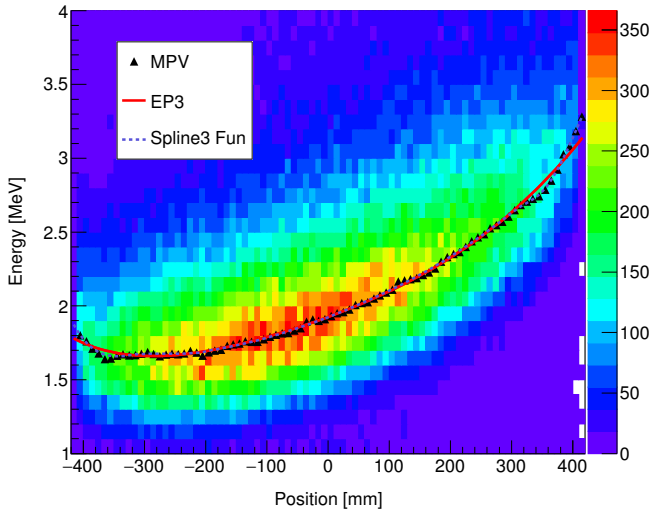


**Fig. 12** Energy of minimum-ionizing protons (vertical axis) versus the hit position (horizontal axis). The *triangles* are the MPV values of the energy distributions for the bins of the horizontal axis, the *red solid line* is the fit-function as Equation (3) and the *blue dashed line* is the constructed 3rd-spline function.

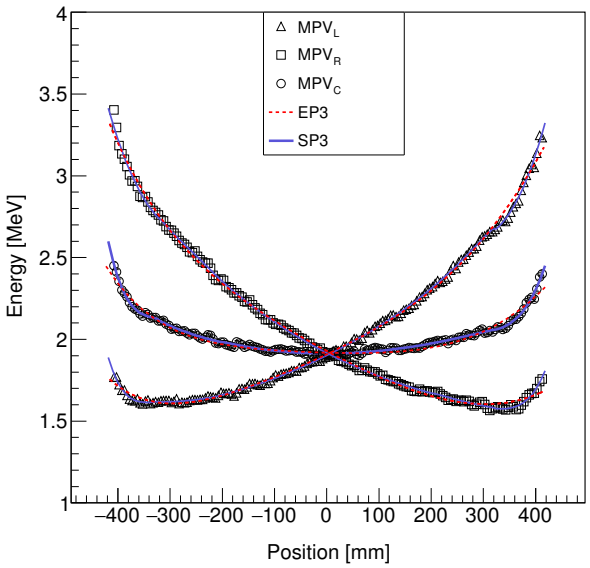


**Fig. 13** MPVs (vertical axis) of right (*triangles*), left (*circles*) and combined (*squares*) side of a PMT versus hit position (horizontal axis). The fitted functions as Equation (3) and constructed spline functions are shown by the *red dashed lines* and the *blue solid lines*, respectively.

($Q_{\rm rec} = Z$). As an example, Figure 15 shows typical data pairs of obtained peak position and charge number (open circles); the constructed third-order spline function and the fitted linear function are depicted by the solid line and dotted line, respectively. The dash-dotted line is the bisector (ordinate = abscissa) as a reference.

As shown by Equation (4), the hit position ($x$) and the path length ($l$) are derived from a selected track. It is common that the track number of an event is greater than one; the situation is much more complicated for the case of high-$Z$ nuclei events. In order to select the right track, one needs to combine the information provided by the PSD, STK and BGO together. Detailed track selection method and reconstruction results will be published in another paper.

## 5 PSD DETECTION EFFICIENCY

Electromagnetic showers can be separated well from hadronic showers by the BGO calorimeter (DAMPE Collaboration et al. 2017). The flux of the cosmic $\gamma$-ray is

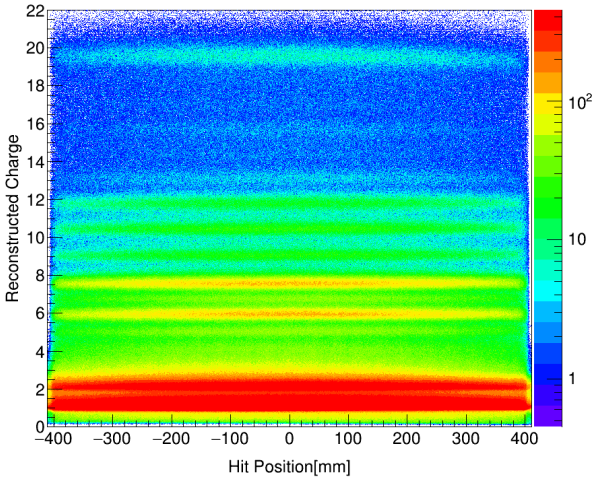


**Fig. 14** Reconstructed charge (vertical axis) versus the hit position (horizontal axis).

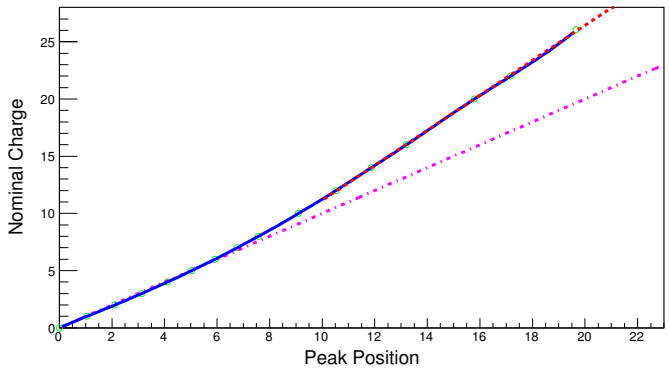


**Fig. 15** Peak positions obtained from a reconstructed charge spectrum versus charge number (*open circles*). The *solid line* and *dotted line* present the constructed third-order spline function and the fitted linear function, respectively, and the *dash-dotted line* is the bisector (ordinate = abscissa) as a reference.

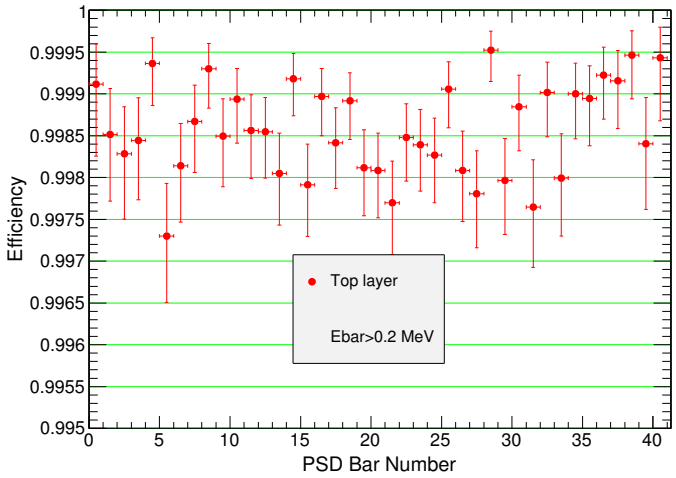


**Fig. 16** The detection efficiency of bars of PSD top layer.

about 1000 times lower than that of electrons. Therefore, the detection efficiency of the PSD is crucial for discriminating the $\gamma$-rays from charged particles. By combining measurements from different sub-detectors, the detection efficiency of each PSD strip can be evaluated. The PSD detection efficiency is investigated by MIP events as well. The detection efficiency of a PSD bar $\eta_{l,b}$ ($l$ and $b$ represent the layer number and strip number, respectively) is defined as follows:

$$\eta_{l,b} = N_{l,b}^{\mathrm{Fired}} / N_{l,b}^{\mathrm{STK}} \ , \tag{5}$$

where $N_{l,b}^{\mathrm{STK}}$ is the number of the global track pointing to the $b$-th strip in the $l$-th layer and $N_{l,b}^{\mathrm{Fired}}$ is the number of the fired PSD bar. The firing condition of a PSD bar is that energies with light attenuation correction in the left and right sides of the bar are larger than 0.2 MeV.

In PSD efficiency evaluation, MIPs events which fulfill the following conditions are used: (a) the event with only one global track; (b) the STK track has five clusters in both the $X$-$Z$ plane and the $Y$-$Z$ plane at least; (c) the reduced $\chi^2(\chi^2/\mathrm{NDF})$ is smaller than 1; (d) the STK track and BGO track are in good agreement. Figure 16 shows the detection efficiency of bars in the top layer of the PSD. The efficiencies of all bars in the X-layer and the Y-layer of the PSD are readily above 99.5%, which is far better than the designed detection efficiency of 95%. The total efficiency of the PSD (at least one PSD bar is fired in the top layer or bottom layer) is evaluated to be above 99.99%.

## 6 SUMMARY

PSD on-orbit calibration procedure including the five steps of pedestal, dynode correlation, MIP response, light attenuation and energy reconstruction are presented in this paper. The on-orbit pedestal, dynode ratio and MIP response of the PSD are verified to be stable. A method for reconstructing the charge of incident particles is introduced including the quenching effect and gain non-linearity corrections. The detection efficiency of the PSD is evaluated with MIPs, the detection efficiency of each PSD bar is large than 99.5%, and the total detection efficiency of the PSD is above 99.99%.

**Acknowledgements** This work was funded by the National Key Research and Development Program of China (2016YFA0400201), and was also supported by the National Natural Science Foundation of China (11673047, 11673075, 11303107, U1738127 and U1738205).

## References

Alpat, B., Ambrosi, G., Azzarello, P., et al. 2005, Nuclear Instruments and Methods in Physics Research A, 540, 121

Atwood, W. B., Abdo, A. A., Ackermann, M., et al. 2009, ApJ, 697, 1071

Azzarello, P., Ambrosi, G., Asfandiyarov, R., et al. 2016, Nuclear Instruments and Methods in Physics Research A, 831, 378

Chang, J., Adams, J. H., Ahn, H. S., et al. 2008, Nature, 456, 362

Chang, J., Ambrosi, G., An, Q., et al. 2017, Astroparticle Physics, 95, 6

DAMPE Collaboration, Ambrosi, G., An, Q., et al. 2017, Nature, 552, 63

Drury, L. O. 2012, Astroparticle Physics, 39, 52

Feng, C., Zhang, D., Zhang, J., et al. 2015, IEEE Transactions on Nuclear Science, 62, 3117

Grenier, I. A., Black, J. H., & Strong, A. W. 2015, ARA&A, 53, 199

He, M., Ma, T., Chang, J., et al. 2016, Acta Astronomica Sinica, 57, 1

Li, Y., Zhang, Y. P., Zhang, Y. J., et al. 2017, Acta Astronomica Sinica, 58, 54

Patrignani, C., & Particle Data Group. 2016, Chinese Physics C, 40, 100001

Picozza, P., Sparvoli, R., & PAMELA Collaboration. 2010, Nuclear Instruments and Methods in Physics Research A, 623, 672

Wang, Y.-P., Wen, S.-C., Jiang, W., et al. 2017, Chinese Physics C, 41, 106001

Winckler, J. R. 1965, Science, 148, 217

Yu, Y., Sun, Z., Su, H., et al. 2017, Astroparticle Physics, 94, 1

Zhang, Z., Zhang, Y., Dong, J., et al. 2015, Nuclear Instruments and Methods in Physics Research A, 780, 21

Zhang, Z., Wang, C., Dong, J., et al. 2016, Nuclear Instruments and Methods in Physics Research A, 836, 98

Zhou, Y., Sun, Z., Yu, Y., et al. 2016, Nuclear Instruments and Methods in Physics Research A, 827, 79